



HHS Public Access

Author manuscript

ACS Nano. Author manuscript; available in PMC 2018 June 27.

Published in final edited form as:

ACS Nano. 2017 June 27; 11(6): 5670–5679. doi:10.1021/acsnano.7b01106.

Breathable Vapor Toxicant Barriers Based on Multilayer Graphene Oxide

Ruben Spitz Steinberg, Michelle Cruz, Naser G. A. Mahfouz[†], Yang Qiu, and Robert H. Hurt^{*}
School of Engineering, Brown University, Providence, Rhode Island 02912, United States

Abstract

There is tremendous interest in graphene-based membranes as protective molecular barriers or molecular sieves for separation technologies. Graphene oxide (GO) films in the dry state are known to be effective barriers for molecular transport and to expand in the presence of moisture to create enlarged intersheet gallery spaces that allow rapid water permeation. Here we explore an application for GO membranes as water-breathable barrier layers for personal protective equipment, which are designed to allow outward perspiration while protecting the wearer from chemical toxicants or biochemical agents in the local environment. A device was developed to measure permeation rates of small-molecular toxicants in the presence of counter-current water flow simulating active perspiration. The technique was applied to trichloroethylene (TCE) and benzene, which are important environmental toxicants, and ethanol as a limiting case to model very small, highly water-soluble organic molecules. Submicron GO membranes are shown to be effective TCE barriers, both in the presence and absence of simulated perspiration flux, and to outperform current barrier technologies. A molecular transport model is developed, which suggests the limited toxicant back-permeation observed occurs not by diffusion against the convective perspiration flow in hydrophobic channels, but rather through oxidized domains where hydrogen-bonding produces a near-stagnant water phase. Benzene and ethanol permeation fluxes are higher than those for TCE, likely reflecting the effects of higher water solubility and smaller minimum molecular dimension. Overall, GO films have high water breathability relative to competing technologies and are known to exclude most classes of target toxicants, including particles, bacteria, viruses, and macromolecules. The present results show good barrier performance for some very small-molecule species, but not others, with permeation being favored by high water solubility and small minimum molecular dimension.

^{*}Corresponding Author: robert_hurt@brown.edu.

[†]Present Address: Department of Chemical Engineering, Carnegie Mellon University, Pittsburgh, PA 15213, United States

Supporting Information

The Supporting Information is available free of charge on the ACS Publications website at DOI: 10.1021/acsnano.7b01106. Figures and sections S1–S9 give more details on film fabrication, analytical techniques, experimental results, model derivations, and GO characterization (PDF)

ORCID

Ruben Spitz Steinberg: 0000-0003-0647-3127

Yang Qiu: 0000-0003-1965-3987

Robert H. Hurt: 0000-0002-2036-9337

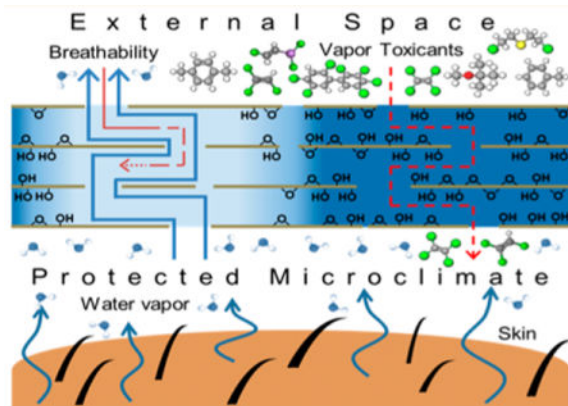
Author Contributions

R.H.H. and R.S.S. designed the experiments and wrote the manuscript. R.S.S., M.C., N.G.A.M., and Y.Q. conducted the experiments.

Notes

The authors declare no competing financial interest.

Graphical abstract



Keywords

graphene oxide; chemical protection; breathability; smart fabrics; selective membranes

An exciting application area for emerging materials is in multifunctional or “smart” fabrics.^{1–7} The “multifunctional” label applies to technologies that combine two or more features, which may include skin protection, environmental sensing, controlled release, active temperature regulation, dynamic photonic behaviors, or mechanical or solar energy harvesting.^{5,6,8} One class of advanced fabric technologies are garments that protect workers or military personnel against environmental toxicants or biochemical agents.^{9–11} A major challenge for such barrier fabrics is body temperature regulation.^{9,12–14} A significant heat loss mechanism in humans is perspiration with endothermic evaporation, and this relies on efficient transport of water vapor from the microclimate between the skin surface and fabric to the atmosphere. Conventional barrier materials typically inhibit water vapor flux, leading to overheating and severe limitations on the duration of use, especially in warm weather environments or during strenuous activity.^{9,12–14}

Many other fabric types are highly porous and thus intrinsically breathable, but do not offer protection against environmental toxicants. The materials challenge is to simultaneously achieve both barrier performance and water breathability in the same material, and the difficulty overcoming this challenge reflects the conflicting requirements for an active layer to show both high water-vapor permeability and high toxicant rejection. This is a significant area for active technological innovation. Some protective garment concepts include personal ventilation fans for active water-vapor release,¹⁵ but this increases the bulk and weight of the garment. A recent example of a proposed advanced technology in the area of breathable barriers is a composite material incorporating vertically aligned single-walled carbon nanotubes embedded in the polymer polyethylene-N.¹⁶ This technology exploits the rapid water flow in nanotube cores and their well-defined inner diameters as a mechanism for toxicant rejection by size exclusion.¹⁶ In general, materials that show *selective* permeation of water over other substances may be promising candidates for active layers in breathable toxicant barriers.

Recent work has shown graphene oxide (GO) multilayer films to be highly permeable to water.¹⁷ Exposure to either liquid water or humid air causes spontaneous H₂O intercalation into GO films, expanding their interlayer spacing from ~6 Å to ~8–12 Å depending on specific hydration conditions,^{17–20} and allowing near-frictionless liquid water flow through internal hydrophobic channels.^{17,21–24} This original report of “unimpeded” water flow through GO films by Nair *et al.*¹⁷ has been followed by numerous studies exploring various applications of the behavior, including pervaporation membranes,^{25,26} water filtration,^{27–30} separation of aqueous solutions,²¹ and others.³¹ GO films and composites have also been used for gas separation,^{32–35} and dry GO or reduced GO have been evaluated as absolute (nonselective) molecular barriers.^{36–39} We are not aware, however, of studies evaluating GO membranes as active layers in breathable vapor toxicant barrier technologies.

There is reason to expect that GO films will be attractive as breathable barriers. First, in the dry state, multilayer GO films have been reported to reject all molecules, including He atoms, if fabricated to be thicker than about ~20 nm.^{36,37} Above this thickness threshold, the collection of deposited GO nanosheets can completely cover an underlying substrate without significant gaps from the random sheet tiling process or stacking defects³⁶ and show excellent barrier performance.^{36,37} Under wet conditions, these GO films expand to create fine channels and become molecular sieves, and liquid-phase permeation studies show that wet GO membranes reject molecules or ions with hydrated radii larger than 4.5 Å²² (>9 Å molecular size), which are too large to penetrate GO gallery spaces even after water-induced interlayer expansion. Thin GO films are also flexible⁴⁰ and highly resistant to chemical dissolution or corrosion,³⁷ which are favorable characteristics for practical barrier layer technologies.

The present work evaluates GO films as barriers to vapor-phase toxicants and focuses on three key questions: (i) the breathability (to water vapor) relative to established standards and competing materials; (ii) the permeation rates of target vapor toxicants under hydrated film conditions with expanded interlayer spaces; and (iii) permeation rates and behaviors in the presence of active outward water flux (simulated perspiration). To address issue (ii), we chose trichloroethylene (TCE) as a model of a small-molecule vapor toxicant, with a kinetic diameter of 5.6 Å.⁴¹ TCE has been used as an intermediate for the manufacture of HFC-134a refrigerant, as a degreasing solvent, and in a variety of consumer products such as sealants, lubricants, and pepper spray.^{42,43} TCE is now a high-priority volatile organic toxicant found at many waste sites; as a dense nonaqueous phase liquid, it can reach bedrock below the water table, be transported over long distances, and contaminate large volumes of water for extended periods of time.⁴⁴ As a result, TCE presents a vapor intrusion risk by volatilization, upward vapor transport, and penetration of aboveground structures even at significant distances from the original site of contamination.⁴⁵ From a human health perspective, it has been characterized as carcinogenic, toxic to the nervous, respiratory, hepatic, renal, immune, and reproductive systems, and as a developmental toxicant.^{42,43} We also include data on benzene (5.9 Å),⁴⁶ which is also an important environmental toxicant and human carcinogen, but unlike TCE is a light (low-density) nonaqueous phase liquid with disk-shaped molecular structure, and ethanol (4.4 Å⁴⁷) as a model for small and water-soluble organic molecules such as formaldehyde or sarin.^{48–50} To address issue (iii) will require specialized testing of GO film permeation in the presence and absence of controlled

gradients in water vapor concentration, for which a custom device was built, validated, and used for this study.

RESULTS AND DISCUSSION

GO suspensions were made by a modified Hummers' method and cast into uniform multilayer films (Figure 1) by positive pressure filtration²⁶ onto a porous polycarbonate membrane (see Methods). Polycarbonate was chosen over anodized aluminum oxide in order to prevent uncontrolled cross-linking by leached aluminum ions.⁵¹ Film thicknesses were calculated from solution volume and GO concentration using d -spacings for hydrated GO measured by X-ray diffraction (XRD), which were consistent with literature reports (see Section S1 of the SI).^{52–54} Selected film thicknesses were confirmed directly by atomic force microscopy (AFM) (Figure 1f), confirming accurate control over GO film thickness. X-ray photoelectron spectroscopy (XPS), Raman spectroscopy, and Fourier transform infrared spectroscopy (FTIR) analyses of the GO starting material are provided in Figure 1b–d, and show the characteristic spectra for GO with a C:O atomic ratio of ~2.1. AFM was used to confirm the primary monolayer/bilayer form of the stock suspension (Figure 1e).

Significant effort was expended to develop a custom diffusion cell for measuring toxicant vapor permeation in the presence of controlled gradients in water vapor concentration to create conditions that simulate perspiration. Of particular interest is a scenario with near-saturated water vapor on one side of the GO membrane, representing the microclimate in the skin–fabric gap space and the vapor toxicant on the other side coexisting with lower concentrations of water vapor, representing a contaminated environment with variable humidity. The device must provide this H₂O-concentration gradient across the film to drive simulated perspiration, while allowing for measurement of counter-current flux of TCE or benzene or ethanol. Figure 2 shows the device, which consists of an inner vessel containing a liquid water inventory that is the source of the simulated perspiration and also serves as a receptacle for collecting and analyzing the permeated TCE, benzene, or ethanol. The inner vessel is capped with a copper plate outfitted with a 1 cm hole for the GO films and O-ring seals (Figure 2 center). An outer vessel creates the simulated atmosphere and is placed in a thermostatic bath to control temperature and vapor pressure of all components. Both the inner and outer vessels are mechanically stirred to minimize transport resistances in the gas spaces above and below the film and thus isolate the true film resistance and permeability for direct measurement. The composition of the simulated atmosphere is controlled by passing compressed dry air through a liquid column of the volatile model toxicant under temperature control to set the vapor pressure of the air-toxicant mixture entering the outer chamber (Figure 2 top). The external humidity was controlled by adding aqueous salt solutions to the outer chamber in selected experiments. Water permeation was measured gravimetrically, while the (generally much lower) toxicant fluxes were determined from measurements of toxicant concentration in the downstream receiving pool of liquid water at the end of the experiment (see Methods and Figure S3). Those concentrations multiplied by solution volume and divided by the experimental time and membrane cross section are reported as the average counter-current flux.

Before starting multicomponent permeation experiments, the device and GO film fabrication method were tested with simple single-component liquids for validation. Using pure hexane liquid at $T = 20\text{ }^{\circ}\text{C}$ as the source, which is known to be rejected by size exclusion in dry GO films,²² no mass loss was detected through dry 10 nm-thick or 1000 nm-thick films after 6 h. This confirms the lack of cracks or pores in the GO films and the quality of the device seals. Using pure liquid water at $T = 60\text{ }^{\circ}\text{C}$ as the source led to permeation at a rate of $4 \times 10^4\text{ g m}^{-2}\text{ day}^{-1}$, similar to the earlier reports of Nair *et al.*¹⁷

Figure 3 summarizes the data on toxicant permeation in complex environments containing water vapor. Figure 3a shows the primary data in its original form, as time-resolved concentrations of organic toxicant in the inner water reservoir. Figure 3b shows the corresponding molecular fluxes for GO films of variable thickness (10–1000 nm). The water data are shown as flux upward from the liquid H₂O source and on the right-hand axis in the alternative units traditionally used to describe breathability in fabrics and membranes ($\text{g m}^{-2}\text{ day}^{-1}$). These water fluxes are measured in the presence of back-diffusing TCE (set at 184 mbar, or 0.93 g/L vapor), benzene (set at 242 mbar, or 0.73 g/L vapor), or ethanol (set at 178 mbar, or 0.32 g/L vapor). The water fluxes are not strongly dependent on film thickness, indicating that transport within the gas spaces rather than diffusion in the GO films is the rate-limiting step. This reflects the very low resistance to water transport within GO films and is similar to the behavior reported elsewhere.¹⁷ The water flux data can also be compared to the commonly cited minimum (threshold) flux of $2000\text{ g m}^{-2}\text{ day}^{-1}$ that defines a breathable fabric^{9,12–14} (see dashed line) and to results from a recent report on a carbon nanotube-based breathable barrier technology also under development at the laboratory scale.¹⁶ Note the water fluxes reported here are for saturated water vapor at $60\text{ }^{\circ}\text{C}$ and, due to the temperature dependence of vapor pressure, can be a factor of ~ 3 higher than fluxes measured at $37\text{ }^{\circ}\text{C}$. It is clear that these GO films show very high breathability relative to current industry practice and are competitive with other material systems under development.

TCE back-diffusion fluxes are 4–5 orders of magnitude lower than the perspiration water fluxes (Figure 3b). The fluxes are highly dependent on film thickness, indicating that transport within the GO film is a significant resistance that governs the overall rate. A full transport model developed later will show that the GO film is the major, rate-limiting resistance under these conditions, consistent with the presence of active stirring in the gas spaces above and below the film. To test the effect of the counter-current simulated perspiration, water vapor was introduced to the outer chamber at a controlled vapor pressure matching that of the inner chamber to stop the water flow while maintaining wet conditions in the film. This increases TCE flux by a factor of 3.8, demonstrating that the counter-current water flow is a significant factor in preventing TCE permeation. Ethanol back-permeation rates are also thickness dependent, but much higher than TCE, with benzene showing intermediate behaviors. We note in Figure 3 that the overall selectivity ratios (water flux/organic flux) increase with increasing film thickness. We do not believe that thicker films are intrinsically more selective, but rather that water flux is “pinned” at a near constant value since the resistance to water flow in the film is so low that external mass transfer to the bottom of the film or from the top of the film becomes rate limiting.

Figure 4 shows TCE permeabilities measured here and comparisons to literature values for other engineered barrier films. The engineered barriers include chlorobutyl rubber with nanoclay fillers for enhanced barrier function⁵⁵ and composite geo-membranes specifically designed to mitigate intrusion of volatile organic compounds into buildings.^{56,57} At equal thickness, GO membranes show the best TCE barrier performance and would have a strong advantage for ultrathin or ultralight applications as they maintain good barrier performance below 100 nm thickness.

A mathematical transport model was developed to better understand the complex toxicant permeation behavior observed experimentally (Figure 3) and its relation to molecular and film properties. A differential, one-dimensional steady-state mass balance was written to describe diffusive molecular flux of a toxicant (“T”) at concentration C_T through a multilayer GO film against a (known) convective flow of liquid water, v :

$$-D_{\text{eff}} \frac{d^2 C_T}{dx^2} = v \frac{dC_T}{dx} \quad (1)$$

Considering the two-phase nature of hydrated GO films (nanosheets and gallery spaces), we expand the apparent properties using a porous media approach:

$$v = v_s \frac{\tau}{\theta}; \quad D_{\text{eff}} = D \frac{\theta}{\tau} k \quad (2)$$

where v_s is the superficial water velocity through the film (volumetric flow per unit film area), v is the local water velocity in the transport channels, τ is a tortuosity factor (actual path length/film thickness), θ is the volume fraction of gallery spaces, D_{eff} the effective diffusivity of T in the film, D the true diffusivity of T in the hydrated channels within the GO film, and k is the aqueous-vapor partition coefficient for substance T. The overlapping, high-aspect-ratio nanosheets give rise to large τ (estimated below), which causes the local water velocity to be much greater than v_s , and the same effect decreases D_{eff} to account for the extended circuitous diffusion path. With these substitutions, one can solve to obtain

$$\dot{N}_T = \frac{C_{T0} \times v_s \left(\frac{\tau}{\theta}\right) e^{-[v_s(\tau/\theta)^2/D \times k \delta]}}{1 - e^{-[v_s(\tau/\theta)^2/D \times k \delta]}} \quad (3)$$

where C_{T0} is the vapor concentration at the upstream face of the film and δ is the film thickness. Note that the diffusion is expected to occur in liquid-like phases within the hydrated gallery spaces of GO multilayer films, but the complex nature of water in GO gallery spaces²⁰ plus nanoconfinement effects make the use of available binary $D_{\text{H}_2\text{O}-\text{T}}$ values for bulk solutions unreliable.³⁶ Note also that the observed flux can be affected by external mass-transfer resistances in the porous polymer backing and/or gas spaces above and below the film. These have been accounted for here using a mass-transfer circuit⁵⁸ with

external resistances accounted for by control experiments in the absence of GO (see Section S5 of the SI).

The simplest application of eq 3 would assume the main toxicant transport occurs through GO gallery spaces, since the hexane data showed no permeation through pinholes or macroscale film defects. The tortuosity can then be estimated as ~ 500 from the GO nanosheet lateral dimension using the Nielsen model,³⁶ and the available volume fraction for transport can be estimated from the hydrated GO film density and the true density. The local water velocity is estimated from the measured water permeation rate (eq 2), assuming liquid-like densities in the gallery spaces. Under these conditions, however, eq 3 predicts no significant back permeation of TCE for any reasonable value of the diffusion coefficient. In essence, the highly tortuous path through the GO gallery spaces implies a very high local water velocity to achieve the observed water flux, and back diffusion is severely restricted due to this counter-current convection plus the elongated diffusion path (note the square dependence on the tortuosity factor in eq 3). The simple model is in clear conflict with the data (Figure S6), which shows a small, but clearly measurable TCE back-permeation rate for all GO films (Figure 3).

To successfully describe the present data set, we needed to extend the simple model to account for an additional diffusive pathway that would allow TCE to back-permeate against the measured water outflow. GO sheets have been reported to consist of distinct domains of oxidized and pristine carbon.⁵⁹ Oxygen-containing functional groups have been reported to undergo spontaneous two-dimensional (2D) migration and clustering, which lowers overall free energy by partially restoring pristine domains of significant size that benefit from extended sp^2 conjugation.⁵⁹ Ultrafast water transport has been attributed to a percolating network of the pristine domains, whose hydrophobic and atomically smooth walls allow near frictionless flow of condensed-phase water.¹⁷ In contrast, the oxidized domains are hydrophilic and prevent frictionless water flow through pinning effects.^{23,24,60} The oxidized domains can be expected to transport water only through much slower “hopping” mechanisms involving the transient formation and breaking of hydrogen-bonds, as occurs in hydrophilic polymers used currently in some dense breathable barrier layers.^{12,61} The hydrophilic domains may also be expected to show some connected, percolating pathways through the film, and since counter-current water transport in those domains is slow, TCE back-permeation may be allowed.

These considerations led to an improved model based on the “segregated domain” concept (Figure 5). Simulated perspiration primarily occurs through near-frictionless convective flow in pristine channels, while toxicant back-transport can occur through two parallel pathways: through the pristine channels against the water flow, or through hydrated oxidized domains with a near-stagnant water phase:

$$\dot{N}_{T, \text{observed}} = \dot{N}_{T, \text{pristine}} + \dot{N}_{T, \text{oxidized}} \quad (4)$$

The first flux component, $\dot{N}_{T, \text{pristine}}$, can still be described by eq 3, though the (τ/θ) parameter can no longer be simply calculated from the bulk film structure, as it represents

only the percolating network of pristine channels. The latter flux component, $\dot{N}_{T, \text{oxidized}}$, can be reasonably modeled as a diffusive process through near-stagnant liquid-water-like layers, but with a much extended path length ($L/\delta = \tau$) created by the presence of the horizontally aligned nanosheet solids:

$$\dot{N}_{T, \text{oxidized}} = \frac{C_{T0}}{\delta} (D \times k)_{\text{oxidized}} \left(\frac{\theta}{\tau} \right)_{\text{oxidized}} \quad (5)$$

where θ_{oxidized} and τ_{oxidized} are the volume fraction and tortuosity for this pathway. Figure 5 shows the model results for TCE permeation using fitted parameters: $(D \times K)_{\text{oxidized}} = 7.3 \times 10^{-6} \text{ cm}^2/\text{s}$, and $(\tau/\theta)_{\text{oxidized}} = 60,000$ with the pristine channel pathway not contributing. Benzene permeation data, on the other hand, is described by $(\tau/\theta)_{\text{pristine}} = 1200$, $(D \times K)_{\text{pristine}} = 1.0 \times 10^{-5} \text{ cm}^2/\text{s}$, $(\tau/\theta)_{\text{oxidized}} = 60,000$, and $(D \times K)_{\text{oxidized}} = 1.0 \times 10^{-3} \text{ cm}^2/\text{s}$. Ethanol back permeation is shown in Figure S8 and is approximately described by $(\tau/\theta)_{\text{pristine}} = 1188$, $(D \times K)_{\text{pristine}} = 1.0 \times 10^{-4} \text{ cm}^2/\text{s}$, $(\tau/\theta)_{\text{oxidized}} = 50,000$, and $(D \times K)_{\text{oxidized}} = 1.9 \times 10^{-2} \text{ cm}^2/\text{s}$. The large τ/θ values were expected, as they reflect the highly tortuous path around the 2D nanosheets, and are similar for all three molecules, which is also expected since they are geometric film parameters and not molecular properties.

Based on the results in Figure 5, the inclusion of the stagnant water pathway through oxidized domains can easily explain the observed TCE/benzene/ethanol breakthrough, while still allowing rapid outward flux of the simulated perspiration. The concept of multiple transport pathways through GO films has support in a number of recent studies on different film applications.^{24,27,59,62} Some studies postulate a pathway associated with film defects or pores,^{24,59} but our analysis did not require the explicit consideration of such a pathway. The hexane exclusion results suggest this pathway is small for our films, and any effect of film defects is likely subsumed by the oxidized domain pathway, which we believe is highly significant for small-molecule back-permeation under these conditions.

The success of the segregated domain model (Figure 5) now allows us to query the final model parameters to seek insight into the molecular properties and film properties that govern toxicant permeation. Regarding the two parallel pathways, the final model parameters predict that the pristine channel pathway, $\dot{N}_{T, \text{pristine}}$, is negligible for all benzene and ethanol experiments except with the thinnest films ($\sim 10 \text{ nm}$) and for all TCE experiments at all film thicknesses. The convective water flow under these conditions (from a saturated vapor source) is too great for diffusive flux in the opposite direction to break through to the back side of the film. Almost all of the TCE, benzene, and ethanol permeation occurs through the oxidized domain pathway. Second, we were interested in the molecular mechanisms responsible for the much lower permeation rates of TCE relative to ethanol. Using eq 5, the fluxes for the thicker films are proportional to $(D \times K)_{\text{oxidized}} \times (\theta/\tau)_{\text{oxidized}}$, and it may be reasonable to assume that the channel geometries are similar for the two molecules, thus $(\theta/\tau)_{\text{oxidized}}$ is expected to be similar. For 100 nm films, TCE fluxes are over 3 orders of magnitude lower than those for ethanol, and the explanation likely lies in $(D \times K)_{\text{oxidized}}$ ratios. For bulk water at 60 °C, the partition coefficients ($C_{\text{bulk water}}/C_{\text{vapor}}$) are

readily found in the literature and are 0.7 for TCE,⁶³ 0.9 for benzene,⁶⁴ and 486 for ethanol⁶⁵ for ratios of about 1.3 and 700, respectively. Although bulk water values are not quantitatively reliable in the nanoconfined hydrated GO gallery spaces, these ratios suggest that vapor-solution partitioning (related to water solubility) accounts for a major portion of the observed differences in toxicant fluxes. In contrast, molecular diffusivities in bulk water are similar for TCE ($1.1 \times 10^{-5} \text{ cm}^2 \text{ s}^{-1}$ at 60 °C),^{66,67} benzene ($1.2 \times 10^{-5} \text{ cm}^2 \text{ s}^{-1}$ at 60 °C),^{66,68} and ethanol ($2.0 \times 10^{-5} \text{ cm}^2 \text{ s}^{-1}$ at 60 °C),⁶⁹ which further supports differences in k as a main mechanism for the higher permeability of ethanol. The significantly higher flux of benzene relative to TCE may also reflect molecular shape differences. While both are planar molecules with similar kinetic diameters (5.6 Å for TCE⁴¹ and 5.9 Å for benzene⁴⁶), benzene is disk-like and thinner than TCE in the Z direction (3.3 Å⁷⁰ vs 3.6 Å^{71,72}), which may facilitate its diffusion in the slot-like GO galleries.

A mechanistic explanation for the selective permeation behavior can be summarized based on the present and prior studies. In the dry state, the GO film interlayer spacings are too small to allow permeation of any molecule.¹⁷ The oxygen-containing domains come into direct vdW contact, leaving no interlayer pore. In principle, the pristine domains do form pores as they are separated from each other by pillaring effects of the neighboring oxidized domains. The size of these pristine domain pores can be estimated as the measured GO interlayer spacing (~0.6 nm) minus the width of the two π -electron clouds (0.34 nm) giving 0.6–0.34 = ~0.26 nm, which is smaller than all known molecules. Dry GO films without pinholes are thus impermeable.^{17,23,24}

In the presence of water, however, there is spontaneous H₂O intercalation and swelling driven by hydrogen-bonding with the hydrophilic O-containing groups, and interlayer spaces increase to 0.8–1.2 nm depending on hydration conditions.^{18,19} This creates hydrophilic pores near the oxygenated domains and hydrophobic channels associated with pristine domains. These latter channels can have sizes that reach $\sim 1.2 - 0.34 = 0.86$ nm and can pass liquid-like water in near frictionless flow.^{17,19} Since water is now abundant, other species can take advantage of the enlarged spaces and permeate, but must be transported through these very fine and fully hydrated pores of high tortuosity.²² This is a much slower process as these species act as solutes that compete with water for the channel cross section, and permeation is favored by water solubility, which increases local concentration of diffusing species, and small molecular size allowing penetration and mobility in the gallery spaces.

CONCLUSIONS

Multilayer GO films are promising candidates for breathable barrier layers in protective fabrics. Their breathability (standard water permeation rates) is far above the threshold requirement of $2000 \text{ g m}^{-2} \text{ day}^{-1}$ and is competitive or superior to other technologies under development. As barriers, properly structured multilayer GO films are known to sterically exclude substances larger than 0.9 nm diameter²² and would be effective barriers against bacteria, viruses, aerosol particulate, and most molecular agents. For small molecule toxicants in vapor phase, experimental results here on films of 10–1000 nm thickness show good barrier performance against trichloroethylene (fluxes $< 10^{-10} \text{ mol/cm}^2 \cdot \text{s}$), but less effective barrier performance against benzene (fluxes $< 10^{-8} \text{ mol/cm}^2 \cdot \text{s}$) and especially

ethanol (fluxes $<10^{-6}$ mol/cm²·s) under conditions of active perspiration. Below 10 nm thickness, it becomes difficult to create films free of macro-defects due to stacking faults or pin holes. A model of small-molecule transport in hydrated GO films suggests that the difference is primarily related to water solubility (vapor-aqueous partition coefficients) and molecular size/shape, which affect toxicant concentrations and movement within the hydrated films. More work is needed to confirm this structure–property relationship over a range of target toxicants, but the present result suggests we can expect good barrier performance for low-water-solubility environmental toxicants such as hydrocarbons, dioxins, elemental mercury, PCBs, and perchlorethylene, but less effective barrier performance for very small, water-soluble toxicants, such as formaldehyde (2.4 Å diameter,⁴⁸ fully miscible) or sarin (size 6.96 Å,⁵⁰ fully miscible⁴⁹). Incorporation of graphene oxide nanosheets, or any engineered nanomaterial, into clothing may raise safety issues,^{73,74} though in multilayer stacked films the bioavailability of individual respirable nanosheets is likely to be low. More work is also recommended on mechanical properties, incorporation in multilayer constructs, and wear-induced nanosheet release. Finally, graphene-based layers may offer additional advantages or functions in smart fabrics such as UV absorption⁷⁵ or stretchability, which can be achieved in these ultrathin films by controlled prewrinkling or precrumpling as demonstrated in recent studies.^{40,76}

METHODS

Materials

Graphite powder (SP-1) was purchased from Bay Carbon Inc. Potassium persulfate, phosphorus pentoxide, potassium permanganate, and trichloroethylene (all ACS reagent grade) were purchased from Sigma-Aldrich. Hydrochloric acid, sulfuric acid, and hydrogen peroxide (all ACS reagent grade) were purchased from Fisher Scientific. Ethanol, acetone, benzene, and hexane (all ACS reagent grade) were purchased from Pharmaco Aaper. All reagents were used as received without further purification. Copper sheets (0.3 mm thick) and ethyl cyanoacrylate adhesives were purchased from McMaster Carr. Track-etched polycarbonate membranes, 6 μm thick with 0.05 μm pores were purchased from GE Life Sciences. All water used was deionized to 18.2 MΩ·cm.

Fabrication of Polycarbonate-Supported GO Films

GO aqueous suspensions were prepared by a modified Hummers method and purified and characterized as described previously.⁷⁷ GO films were formed on porous polycarbonate membranes by positive pressure filtration from aqueous GO suspensions. Fixed volumes of GO suspensions of selected concentrations (0.3–30 μg/mL) were filtered through track-etched polycarbonate membranes using compressed air at 40 psi to ensure consistent GO interlayer spacing (*d*-spacing) from sample to sample.²⁶

Characterization

Surface morphology of GO films was characterized by AFM (Asylum MFP-3D Origin) operating in alternating contact mode. Transmission electron microscopy was performed with a JEOL 2100F TEM/STEM operating at 200 keV using lacey carbon supported samples. XRD spectrometry was carried out on a Bruker AXS D8 with Cu KR radiation, λ

= 1.5418 Å; films were soaked in different media overnight before commencing with the XRD analysis. XPS analysis was performed using a Thermo Scientific K-Alpha XPS. Raman spectroscopy was performed on a Witec Alpha 300 Confocal Raman Microscope. FTIR spectroscopy was performed on a Jasco Instruments FT/IR-4100 with an ATR PRO450-S attenuated total reflectance cell.

Molecular Permeation Studies

A custom device was developed for studying molecular vapor permeation through GO films under wet or dry conditions and in the presence or absence of active water transport simulating perspiration flux (Figure 2). Simulated perspiration flux was controlled by setting water vapor partial pressures on both sides of the membrane, and the true film transport resistance was isolated by minimizing external resistances through convective stirring in the liquid source and outer chamber gas space. The test membranes (polycarbonate-supported GO films) were adhered over a 1 cm diameter hole in a thick copper sheet and partially covered with a ring of aluminum foil; samples were allowed to dry overnight. The water source was loaded in the thermostated device and preheated to 60 °C to set vapor pressure (the elevated temperature both accelerates the experiments and allows stable temperature regulation), while a 1 L per minute stream of extra dry air was flowing to stabilize concentrations gradients. After the temperature is established, the internal vessel was sealed with the copper-mounted GO sample using o-rings and an open glass cover; this setup was weighed, and the seal was tightened using a pinch clamp and returned to the outer chamber. The stream of extra dry air was then redirected through a temperature-controlled sparger filled with the volatile test substance and introduced into the outer chamber with mechanical stirring. After 6 h, the remaining mass was recorded again, and the contents of the beaker were collected and stored for chemical analysis.

TCE containing aqueous samples were analyzed using a Shimadzu GC-2010 with a Restek Rxi-624Sil MS column following the US EPA 551.1 method. Benzene containing aqueous samples were analyzed using a Jasco Instruments V-730 spectrophotometer. Ethanol containing aqueous samples were analyzed using a Jasco Instruments FT/IR-4100 with an ATR PRO450-S attenuated total reflectance cell.

Statistical Analysis

Selected samples were run in triplicates, and the standard deviations for the analytical results were used to generate and present error bars.

Supplementary Material

Refer to Web version on PubMed Central for supplementary material.

Acknowledgments

We acknowledge financial support from the Superfund Research Program of the National Institute of Environmental Health Sciences, grant 2P42 ES013660. We also acknowledge the help of Professor Gerald J. Diebold in creating custom glass components used in this study.

References

1. Coyle S, Wu Y, Lau K-T, De Rossi D, Wallace G, Diamond D. Smart Nanotextiles: A Review of Materials and Applications. *MRS Bull.* 2007; 32:434–442.
2. Akinwande D, Petrone N, Hone J. Two-Dimensional Flexible Nanoelectronics. *Nat Commun.* 2014; 5:5678. [PubMed: 25517105]
3. Li C, Islam MM, Moore J, Sleppy J, Morrison C, Konstantinov K, Dou SX, Renduchintala C, Thomas J. Wearable Energy-Smart Ribbons for Synchronous Energy Harvest and Storage. *Nat Commun.* 2016; 7:13319. [PubMed: 27834367]
4. Chen J, Huang Y, Zhang N, Zou H, Liu R, Tao C, Fan X, Wang ZL. Micro-Cable Structured Textile for Simultaneously Harvesting Solar and Mechanical Energy. *Nat Energy.* 2016; 1:16138.
5. Lai Y-C, Deng J, Zhang SL, Niu S, Guo H, Wang ZL. Single-Thread-Based Wearable and Highly Stretchable Triboelectric Nanogenerators and Their Applications in Cloth-Based Self-Powered Human-Interactive and Biomedical Sensing. *Adv Funct Mater.* 2017; 27:1604462.
6. Zhai S, Karahan HE, Wei L, Qian Q, Harris AT, Minett AI, Ramakrishna S, Ng AK, Chen Y. Textile Energy Storage: Structural Design Concepts, Material Selection and Future Perspectives. *Energy Storage Mater.* 2016; 3:123–139.
7. Jeong HY, Kim JY, Kim JW, Hwang JO, Kim J-E, Lee JY, Yoon TH, Cho BJ, Kim SO, Ruoff RS, Choi S-Y. Graphene Oxide Thin Films for Flexible Nonvolatile Memory Applications. *Nano Lett.* 2010; 10:4381–4386. [PubMed: 20919689]
8. Honda W, Harada S, Arie T, Akita S, Takei K. Wearable, Human-Interactive, Health-Monitoring, Wireless Devices Fabricated by Macroscale Printing Techniques. *Adv Funct Mater.* 2014; 24:3299–3304.
9. Wartell, MA., Kleinman, MT., Huey, BM., Duffy, LM. Strategies to Protect the Health of Deployed US Forces: Force Protection and Decontamination. The National Academies Press; Washington, DC: 1999.
10. Ford ENJ, Suthiwangcharoen N, D'Angelo PA, Nagarajan R. Role of Single-Walled Carbon Nanotubes on Ester Hydrolysis and Topography of Electrospun Bovine Serum Albumin/Poly(vinyl alcohol) Membranes. *ACS Appl Mater Interfaces.* 2014; 6:11741–11748. [PubMed: 25007411]
11. Srinivasan, S., Lavoie, J., Nagarajan, R. Technical Report NATICK/TR-14/021. Army Natick Soldier Research Development and Engineering Center; Natick, MA: 2014. Data-Driven Property Estimation for Protective Clothing.
12. Lomax GR. Breathable Polyurethane Membranes for Textile and Related Industries. *J Mater Chem.* 2007; 17:2775–2784.
13. Rother M, Barmettler J, Reichmuth A, Araujo JV, Rytka C, Glaied O, Pieleu U, Bruns N. Self-Sealing and Puncture Resistant Breathable Membranes for Water-Evaporation Applications. *Adv Mater.* 2015; 27:6620–6624. [PubMed: 26418974]
14. Gugliuzza A, Drioli E. A Review on Membrane Engineering for Innovation in Wearable Fabrics and Protective Textiles. *J Membr Sci.* 2013; 446:350–375.
15. Lu YH, Wei FR, Lai DD, Shi W, Wang FM, Gao CS, Song GW. A Novel Personal Cooling System (PCS) Incorporated with Phase Change Materials (PCMs) and Ventilation Fans: An Investigation on its Cooling Efficiency. *J Therm Biol.* 2015; 52:137–146. [PubMed: 26267508]
16. Bui N, Meshot ER, Kim S, Peña J, Gibson PW, Wu KJ, Fornasiero F. Ultrabreathable and Protective Membranes with Sub-5 nm Carbon Nanotube Pores. *Adv Mater.* 2016; 28:5871–5877. [PubMed: 27159328]
17. Nair RR, Wu HA, Jayaram PN, Grigorieva IV, Geim AK. Unimpeded Permeation of Water Through Helium-Leak-Tight Graphene-Based Membranes. *Science.* 2012; 335:442–444. [PubMed: 22282806]
18. Lerf A, Buchsteiner A, Pieper J, Schöttl S, Dekany I, Szabo T, Boehm HP. Hydration Behavior and Dynamics of Water Molecules in Graphite Oxide. *J Phys Chem Solids.* 2006; 67:1106–1110.
19. Cerveny S, Barroso-Bujans F, Alegría Á, Colmenero J. Dynamics of Water Intercalated in Graphite Oxide. *J Phys Chem C.* 2010; 114:2604–2612.

20. Zhu J, Andres CM, Xu J, Ramamoorthy A, Tsotsis T, Kotov NA. Pseudonegative Thermal Expansion and the State of Water in Graphene Oxide Layered Assemblies. *ACS Nano*. 2012; 6:8357–8365. [PubMed: 22861527]
21. Huang K, Liu GP, Lou YY, Dong ZY, Shen J, Jin WQ. A Graphene Oxide Membrane with Highly Selective Molecular Separation of Aqueous Organic Solution. *Angew Chem, Int Ed*. 2014; 53:6929–6932.
22. Joshi RK, Carbone P, Wang FC, Kravets VG, Su Y, Grigorieva IV, Wu HA, Geim AK, Nair RR. Precise and Ultrafast Molecular Sieving Through Graphene Oxide Membranes. *Science*. 2014; 343:752–754. [PubMed: 24531966]
23. Sun PZ, Liu H, Wang KL, Zhong ML, Wu DH, Zhu HW. Ultrafast Liquid Water Transport Through Graphene-Based Nanochannels Measured by Isotope Labelling. *Chem Commun*. 2015; 51:3251–3254.
24. Wei N, Peng XS, Xu ZP. Understanding Water Permeation in Graphene Oxide Membranes. *ACS Appl Mater Interfaces*. 2014; 6:5877–5883. [PubMed: 24669772]
25. Li GH, Shi L, Zeng GF, Li M, Zhang YF, Sun YH. Sharp Molecular-Sieving of Alcohol-Water Mixtures Over Phenylidiboronic Acid Pillared Graphene Oxide Framework (GOF) Hybrid Membrane. *Chem Commun*. 2015; 51:7345–7348.
26. Tang YP, Paul DR, Chung TS. Free-Standing Graphene Oxide Thin Films Assembled by a Pressurized Ultrafiltration Method for Dehydration of Ethanol. *J Membr Sci*. 2014; 458:199–208.
27. Han Y, Xu Z, Gao C. Ultrathin Graphene Nanofiltration Membrane for Water Purification. *Adv Funct Mater*. 2013; 23:3693–3700.
28. Mi BX. Graphene Oxide Membranes for Ionic and Molecular Sieving. *Science*. 2014; 343:740–742. [PubMed: 24531961]
29. Chen XF, Qiu MH, Ding H, Fu KY, Fan YQ. A Reduced Graphene Oxide Nanofiltration Membrane Intercalated by Well-Dispersed Carbon Nanotubes for Drinking Water Purification. *Nanoscale*. 2016; 8:5696–5705. [PubMed: 26898192]
30. Amadei CA, Vecitis CD. How to Increase the Signal-to-Noise Ratio of Graphene Oxide Membrane Research. *J Phys Chem Lett*. 2016; 7:3791–3797. [PubMed: 27706942]
31. Goh K, Karahan HE, Wei L, Bae T-H, Fane AG, Wang R, Chen Y. Carbon Nanomaterials for Advancing Separation Membranes: A Strategic Perspective. *Carbon*. 2016; 109:694–710.
32. Shen J, Liu GP, Huang K, Chu ZY, Jin WQ, Xu NP. Subnanometer Two-Dimensional Graphene Oxide Channels for Ultrafast Gas Sieving. *ACS Nano*. 2016; 10:3398–3409. [PubMed: 26866661]
33. Kim WG, Nair S. Membranes from Nanoporous 1D and 2D Materials: A Review of Opportunities, Developments, and Challenges. *Chem Eng Sci*. 2013; 104:908–924.
34. Kim HW, Yoon HW, Yoon SM, Yoo BM, Ahn BK, Cho YH, Shin HJ, Yang H, Paik U, Kwon S, Choi JY, Park HB. Selective Gas Transport Through Few-Layered Graphene and Graphene Oxide Membranes. *Science*. 2013; 342:91–95. [PubMed: 24092738]
35. Yang YH, Bolling L, Priolo MA, Grunlan JC. Super Gas Barrier and Selectivity of Graphene Oxide-Polymer Multilayer Thin Films. *Adv Mater*. 2013; 25:503–508. [PubMed: 23023816]
36. Guo F, Silverberg G, Bowers S, Kim SP, Datta D, Shenoy V, Hurt RH. Graphene-Based Environmental Barriers. *Environ Sci Technol*. 2012; 46:7717–7724. [PubMed: 22717015]
37. Su Y, Kravets VG, Wong SL, Waters J, Geim AK, Nair RR. Impermeable Barrier Films and Protective Coatings Based on Reduced Graphene Oxide. *Nat Commun*. 2014; 5:4843. [PubMed: 25208890]
38. Berry V. Impermeability of Graphene and its Applications. *Carbon*. 2013; 62:1–10.
39. Nine MJ, Cole MA, Tran DNH, Losic D. Graphene: A Multipurpose Material for Protective Coatings. *J Mater Chem A*. 2015; 3:12580–12602.
40. Wang Z, Tonderys D, Leggett SE, Williams EK, Kiani MT, Spitz Steinberg R, Qiu Y, Wong IY, Hurt RH. Wrinkled, Wavelength-Tunable Graphene-Based Surface Topographies for Directing Cell Alignment and Morphology. *Carbon*. 2016; 97:14–24. [PubMed: 25848137]
41. Alvarez-Cohen L, Mccarty PL, Roberts PV. Sorption of Trichloroethylene onto a Zeolite Accompanied by Methanotrophic Biotransformation. *Environ Sci Technol*. 1993; 27:2141–2148.

42. Chiu WHA, Jinot J, Scott CS, Makris SL, Cooper GS, Dzubow RC, Bale AS, Evans MV, Guyton KZ, Keshava N, Lipscomb JC, Barone S, Fox JF, Gwinn MR, Schaum J, Caldwell JC. Human Health Effects of Trichloroethylene: Key Findings and Scientific Issues. *Environ Health Perspect*. 2013; 121:303–311. [PubMed: 23249866]
43. Environmental Protection Agency. Trichloroethylene (TCE); Significant New Use Rule; TCE in Certain Consumer Products. *Fed Regist*. 2015; 80:47441–47448.
44. Ji SH, Lee HB, Yeo IW, Lee KK. Effect of Nonlinear Flow on DNAPL Migration in a Rough-Walled Fracture. *Water Resour Res*. 2008; 44:44.
45. Yao Y, Shen R, Pennell KG, Suuberg EM. A Review of Vapor Intrusion Models. *Environ Sci Technol*. 2013; 47:2457–2470. [PubMed: 23360069]
46. Baertsch CD, Funke HH, Falconer JL, Noble RD. Permeation of Aromatic Hydrocarbon Vapors Through Silicalite-Zeolite Membranes. *J Phys Chem*. 1996; 100:7676–7679.
47. Chopade VJ, Khandetod YP, Mohod AG. Dehydration of Ethanol-Water Mixture Using 3a Zeolite Adsorbent. *Int J Emerging Technol Adv Eng*. 2015; 5:152–155.
48. Daubert, TE., Danner, RP. *Physical and Thermodynamic Properties of Pure Chemicals: Data Compilation*. Hemisphere Pub Corp; New York: 1989.
49. Stewart, CE. *Weapons of Mass Casualties and Terrorism Response Handbook*. Jones and Bartlett; Sudbury, MA: 2006.
50. Turel, T. Ph.D. Dissertation. Auburn University; Auburn, AL: 2008. Gas Transmission Through Microporous Membranes.
51. Yeh CN, Raidongia K, Shao JJ, Yang QH, Huang JX. On the Origin of the Stability of Graphene Oxide Membranes in Water. *Nat Chem*. 2015; 7:166–170.
52. Acik M, Mattevi C, Gong C, Lee G, Cho K, Chhowalla M, Chabal YJ. The Role of Intercalated Water in Multilayered Graphene Oxide. *ACS Nano*. 2010; 4:5861–5868. [PubMed: 20886867]
53. Mkhoyan KA, Contryman AW, Silcox J, Stewart DA, Eda G, Mattevi C, Miller S, Chhowalla M. Atomic and Electronic Structure of Graphene-Oxide. *Nano Lett*. 2009; 9:1058–1063. [PubMed: 19199476]
54. Talyzin AV, Hausmaninger T, You SJ, Szabo T. The Structure of Graphene Oxide Membranes in Liquid Water, Ethanol and Water-Ethanol Mixtures. *Nanoscale*. 2014; 6:272–281. [PubMed: 24189605]
55. Sridhar V, Tripathy DK. Barrier Properties of Chlorobutyl Nanoclay Composites. *J Appl Polym Sci*. 2006; 101:3630–3637.
56. McWatters RS, Rowe RK. Diffusive Transport of VOCs Through LLDPE and Two Coextruded Geomembranes. *J Geotech Geoenviron Eng*. 2010; 136:1167–1177.
57. McWatters, RS., Rowe, RK. An Investigation of Toluene and TCE Diffusion Through EVOH in Aqueous Solutions; Proceedings from the 10th International Conference on Geosynthetics; Berlin, Germany. September 21–25, 2014; Jupiter, FL: International Geosynthetics Society; 2014.
58. Incropera, FP. *Fundamentals of Heat and Mass Transfer*. John Wiley; Hoboken, NJ: 2007.
59. Erickson K, Erni R, Lee Z, Alem N, Gannett W, Zettl A. Determination of the Local Chemical Structure of Graphene Oxide and Reduced Graphene Oxide. *Adv Mater*. 2010; 22:4467–4472. [PubMed: 20717985]
60. Yoshida H, Bocquet L. Labyrinthine Water Flow Across Multilayer Graphene-Based Membranes: Molecular Dynamics *versus* Continuum Predictions. *J Chem Phys*. 2016; 144:234701. [PubMed: 27334184]
61. Lomax GR. The Design of Waterproof, Water Vapour-Permeable Fabrics. *J Ind Text*. 1985; 15:40–66.
62. Si Y, Samulski ET. Synthesis of Water Soluble Graphene. *Nano Lett*. 2008; 8:1679–1682. [PubMed: 18498200]
63. Heron G, Christensen TH, Enfield CG. Henry's Law Constant for Trichloroethylene Between 10 and 95 °C. *Environ Sci Technol*. 1998; 32:1433–1437.
64. Leighton DT, Calo JM. Distribution Coefficients of Chlorinated Hydrocarbons in Dilute Air-Water Systems for Groundwater Contamination Applications. *J Chem Eng Data*. 1981; 26:382–385.

65. Jones AW. Determination of Liquid Air Partition-Coefficients for Dilute-Solutions of Ethanol in Water, Whole-Blood, and Plasma. *J Anal Toxicol.* 1983; 7:193–197. [PubMed: 6101261]
66. Reid, RC., Prausnitz, JM., Poling, BE. *The Properties of Gases and Liquids.* McGraw-Hill; New York: p. 1987
67. Chiao, FF., Currie, RC., McKone, TE., Hsieh, DPH. *Intermedia Transfer Factors for Contaminants Found at Hazardous Waste Sites - Trichloroethylene (TCE).* University of California; Davis, CA: 1994.
68. Chiao, FF., Currie, RC., McKone, TE., Hsieh, DPH. *Intermedia Transfer Factors for Contaminants Found at Hazardous Waste Sites - Benzene.* University of California; Davis CA: 1994.
69. Hayduk W, Laudie H. Prediction of Diffusion Coefficients for Nonelectrolytes in Dilute Aqueous Solutions. *AIChE J.* 1974; 20:611–615.
70. Webster CE, Drago RS, Zerner MC. Molecular Dimensions for Adsorptives. *J Am Chem Soc.* 1998; 120:5509–5516.
71. Li L, Quinlivan PA, Knappe DRU. Effects of Activated Carbon Surface Chemistry and Pore Structure on the Adsorption of Organic Contaminants from Aqueous Solution. *Carbon.* 2002; 40:2085–2100.
72. Karanfil T, Dastgheib SA. Trichloroethylene Adsorption by Fibrous and Granular Activated Carbons: Aqueous Phase, Gas Phase, and Water Vapor Adsorption Studies. *Environ Sci Technol.* 2004; 38:5834–5841. [PubMed: 15573580]
73. Hu XG, Zhou QX. Health and Ecosystem Risks of Graphene. *Chem Rev.* 2013; 113:3815–3835. [PubMed: 23327673]
74. Sanchez VC, Jachak A, Hurt RH, Kane AB. Biological Interactions of Graphene-Family Nanomaterials: An Interdisciplinary Review. *Chem Res Toxicol.* 2012; 25:15–34. [PubMed: 21954945]
75. Qiu Y, Wang Z, Owens ACE, Kulaots I, Chen Y, Kane AB, Hurt RH. Antioxidant Chemistry of Graphene-Based Materials and its Role in Oxidation Protection Technology. *Nanoscale.* 2014; 6:11744–11755. [PubMed: 25157875]
76. Chen P-Y, Sodhi J, Qiu Y, Valentin TM, Spitz Steinberg R, Wang Z, Hurt RH, Wong IY. Multiscale Graphene Topographies Programmed by Sequential Mechanical Deformation. *Adv Mater.* 2016; 28:3564–3571. [PubMed: 26996525]
77. Kim F, Luo JY, Cruz-Silva R, Cote LJ, Sohn K, Huang JX. Self-Propagating Domino-Like Reactions in Oxidized Graphite. *Adv Funct Mater.* 2010; 20:2867–2873.

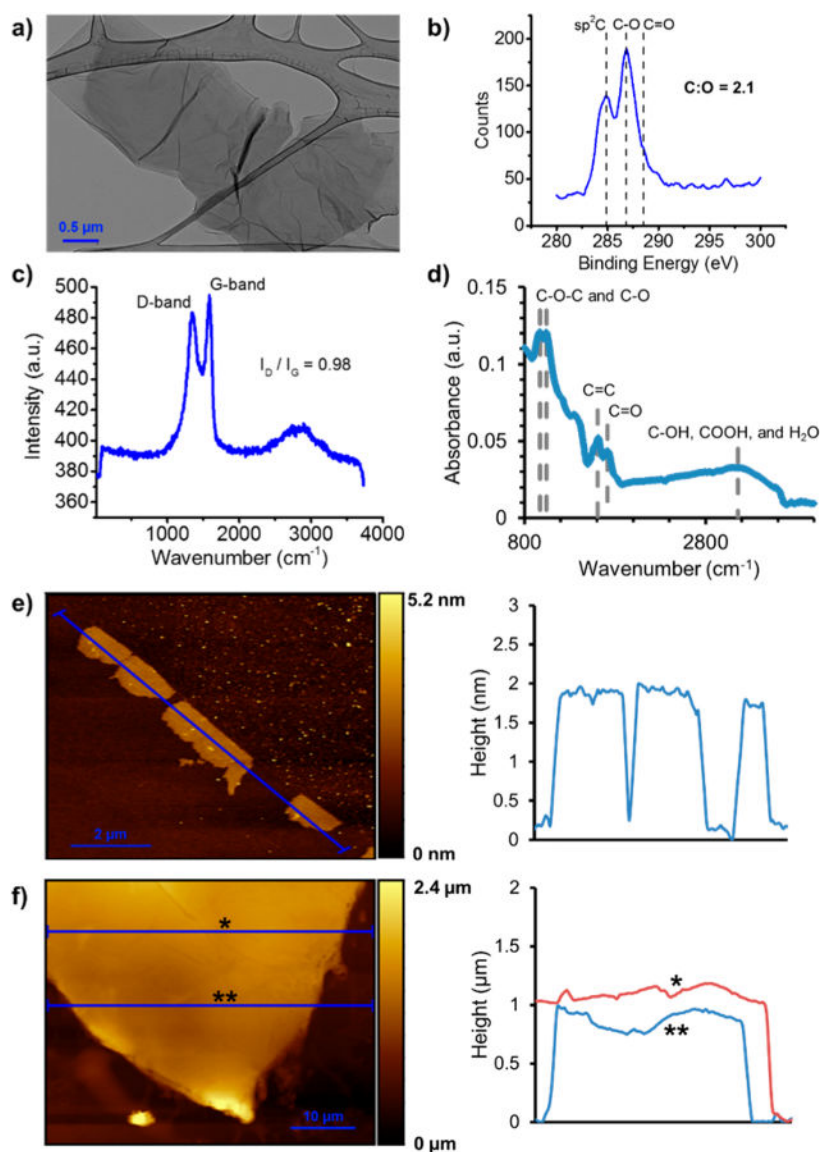


Figure 1. Morphology of GO nanosheets and multilayer films. (a) Transmission electron micrograph (TEM) of typical nanosheet dried from the starting GO suspensions. (b) XPS C 1s characterization of the GO films, showing sp^2C , C–O, and C=O peaks. Elemental analysis gave a GO C:O atomic ratio of ~ 2.1 . (c) Raman spectrum showing a ratio of D- and G-band intensities of 0.98, consistent with XPS results. (d) FTIR spectrum showing the characteristic C–O–C, C–O, C=C, C=O, C–OH, and COOH absorbance peaks for GO. (e) AFM image and accompanying height profile of GO nanosheets drop-cast from diluted suspension onto Si. Shown are mono- or bilayer nanosheets with $\sim 1 \mu\text{m}$ lateral dimension and 1.5–1.8 nm apparent thickness. (f) AFM micrograph and accompanying height profiles of an example $\sim 1 \mu\text{m}$ -thick multilayer film assembled by pressure-driven filtration through a porous polycarbonate membrane, which was subsequently dissolved in methylene chloride to liberate a freestanding film.

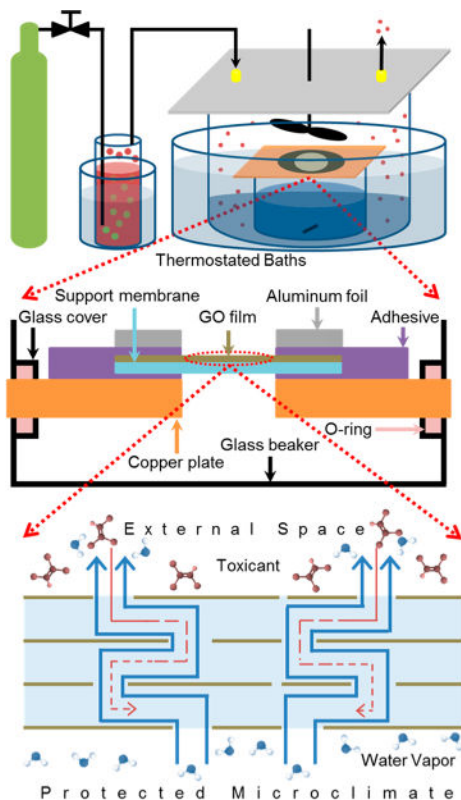


Figure 2. Custom diffusion cell for small-molecule vapor toxicant permeation in the presence of controlled gradients in water vapor concentration. Top: Overall device design with control of gas environments on both sides of a supported GO multilayer film. Middle: Details of the GO film support and sealing system. Bottom: Molecular transport in example experiment with simulated perspiration (H_2O flux in upward direction) and potential simultaneous back-permeation of TCE as a model small-molecule vapor toxicant in the environment.

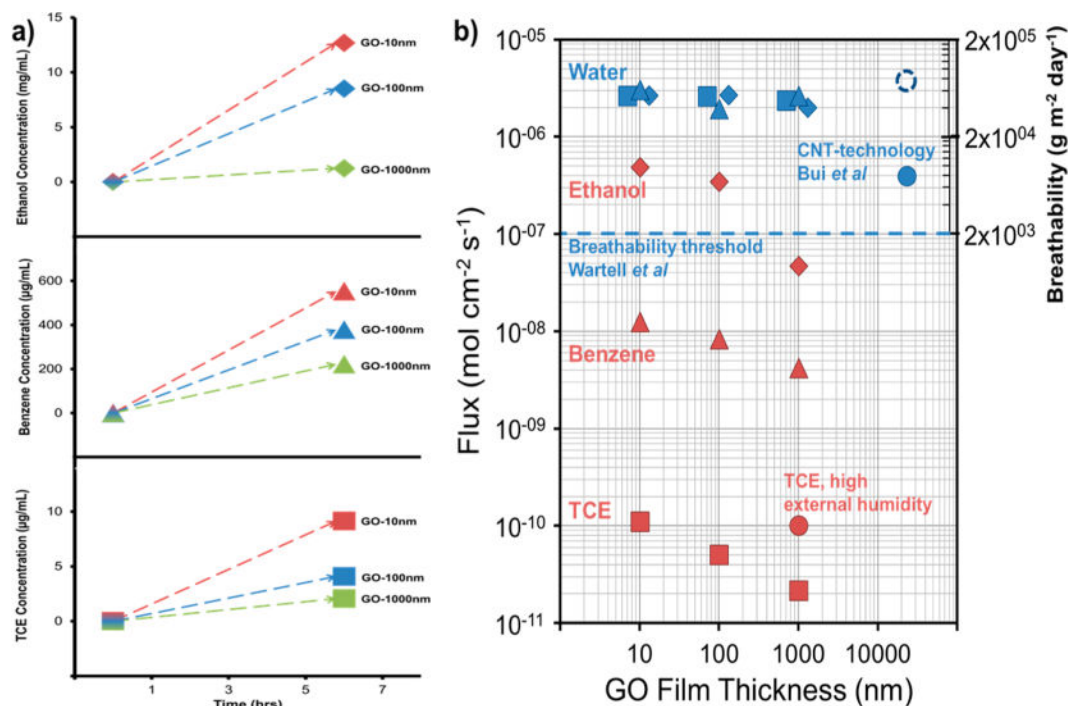


Figure 3.

Experimental results on breathability and barrier functions of GO films. (a) Raw experimental data as time-resolved concentrations in the inner aqueous solution for TCE (bottom), benzene (middle), or ethanol (top). (b) Summary of results in the form of permeation flux in complex multicomponent vapor mixtures. Water data are outward fluxes representing simulated perspiration from a saturated water vapor source (at bottom of film) to dry sweep air (at top of film) at 60 °C and are measured in the presence of back-diffusing TCE (squares), benzene (triangles), or ethanol (diamonds). Literature data and thresholds for breathability provided for reference. Note that the published study on the CNT technology used a lower water vapor concentration (solid circle), and an estimate of the flux at the higher vapor concentrations used in the current study is shown as the dashed circle. Data are for dry air in the external space except where noted. TCE data are inward fluxes measured for 184 mbar TCE partial pressure (above film) to TCE-free space (below film). TCE fluxes were measured either in the presence of active water counter flow (squares) or with the water flow suppressed by addition of water vapor in the outer vessel above the film (circle). Benzene and ethanol data are also inward fluxes and originate from 242 mbar benzene and 178 mbar ethanol vapor partial pressures and measured in the presence of counter flowing simulated perspiration.

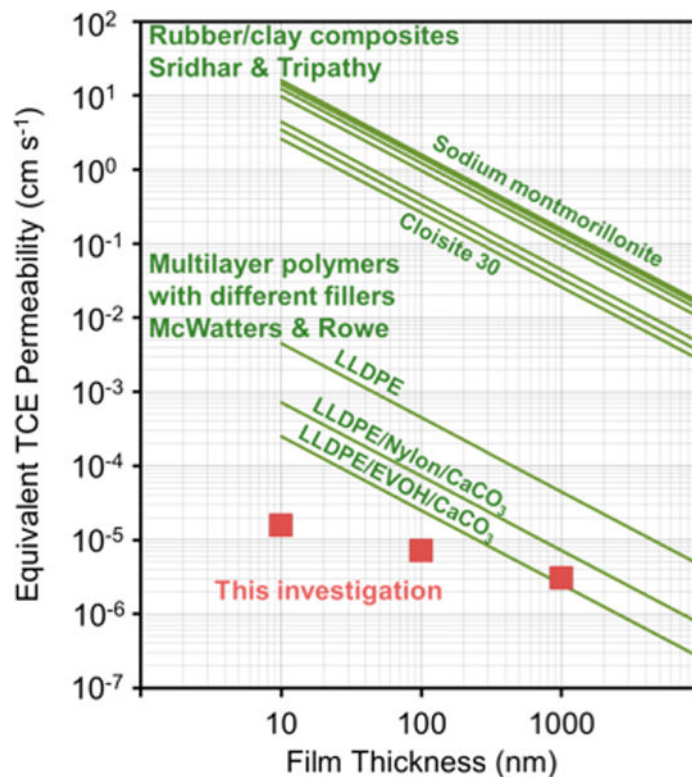


Figure 4.

Comparison of TCE permeabilities for GO films and engineered polymer-matrix barrier films. Red squares are permeability values calculated from flux data in the present study. The upper set of green lines are engineered composite barriers of chlorobutyl rubber with modified or unmodified montmorillonite nanoclays, from Sridhar and Tripathy.⁵⁵ The lower set of green lines are geo-membranes consisting of multiple layers of high- and low-density polyethylene, ethylene vinyl alcohol, and different types of fillers, from McWatters and Rowe.^{56,57} Some literature permeability values were estimated from reported diffusivities (see details in Section S7 of the SI).

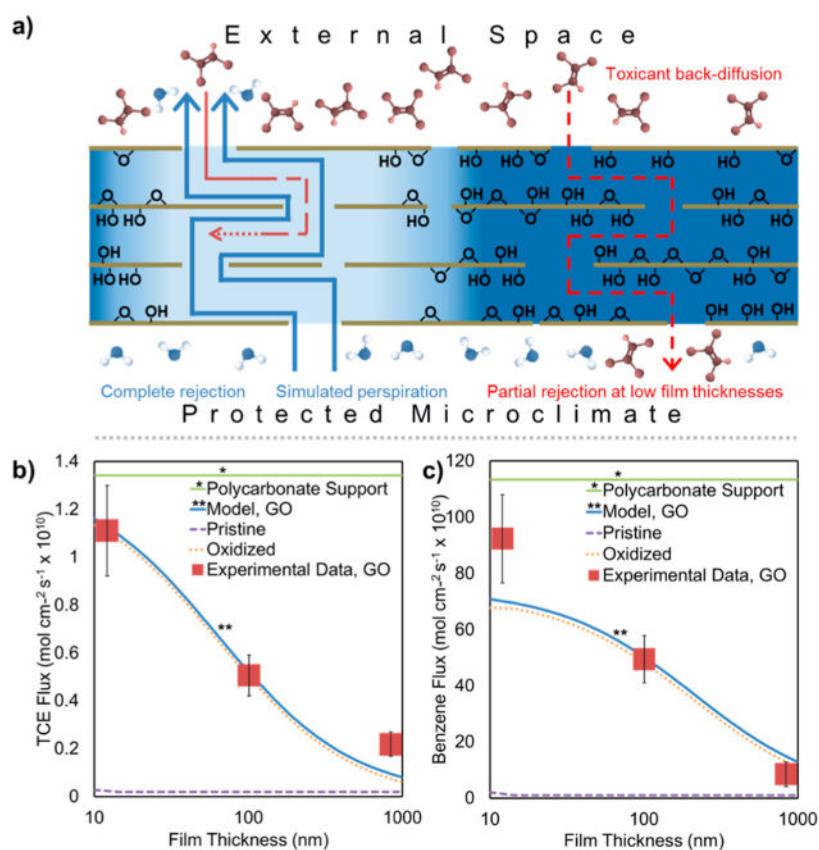


Figure 5. Segregated domain model of molecular permeation through GO films. (a) Conceptual model of perspiration water flow and toxicant back-permeation in GO films with segregated hydrophilic and pristine domains. The primary water flow occurs through near frictionless convection in a percolating network of pristine domains, while the primary toxicant back-permeation occurs through the nearly stagnant hydrated zones in oxidized domains; (b,c) Model-data comparisons for TCE (b) and benzene (c), showing thickness-dependent back-permeation and the relative contributions of the pristine and oxidized pathways.